Nanoscale

Accepted Manuscript

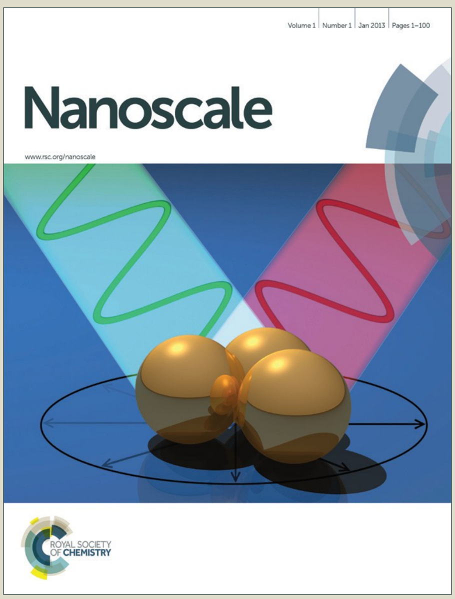

Nanoscale RSCPublishing

ARTICLE

50 nm–sized spherical TiO_2 nanocrystals for highly efficient mesoscopic perovskite solar cells

Cite this: DOI: 10.1039/x0xx00000x

Sang Do Sung,[a] Devi Prashad Ojha,[a] Ji Su You,[a] Joori Lee,[b] Jeongho Kim*[b] and Wan In Lee*[a]

Received 00th January 2012,
Accepted 00th January 2012

DOI: 10.1039/x0xx00000x

www.rsc.org/

Single crystalline TiO_2 nanoparticles (NPs) with spherical morphology are successfully synthesized by hydrothermal reaction in a basic condition. TiO_2 NPs, selectively controlled to the sizes of 30, 40, 50, and 65 nm, are then applied to mesoporous photoelectrode of $CH_3NH_3PbI_3$ perovskite solar cells. In particular, spherical TiO_2 NP of 50 nm size (NP50) offers the highest photovoltaic conversion efficiency (PCE) of 17.19%, with J_{SC} of 21.58 mA/cm^2, V_{OC} of 1,049 mV, and FF of 0.759 while the enhancement of PCE mainly arises from the increase of V_{OC} and FF. Furthermore, the fabricated photovoltaic devices exhibit reproducible PCE values and very little hysteresis in their *J-V* curves. Time-resolved photoluminescence measurement and pulsed light-induced transient measurement of the photocurrent indicate that the device employing NP50 exhibits the longest electron lifetime although the electron injection from perovskite to TiO_2 is less efficient than the devices with smaller TiO_2 NPs. The extended electron lifetime is attributed to the suppression of electron recombination due to optimized mesopores generated by the spherical NP50.

Introduction

Perovskite solar cells that employ methylammonium lead halides ($CH_3NH_3PbX_3$, X=Cl, Br or I) as light absorber have attracted immense interest over the last a few years.[1-17] In particular, $CH_3NH_3PbI_3$ with direct bandgap of 1.5 eV has been regarded as one of the most ideal light absorbers due to its extremely high extinction coefficient, small exciton binding energy, high charge carrier mobility, low expense, and simple processability.[3-8] Accordingly, photovoltaic conversion efficiencies (PCEs) over 16% have been achieved thus far, while it is predicted that higher PCEs over 20% can be reached with further optimization of the materials and devices in the near future.[9-17]

In general, perovskite solar cells are prepared in the form of mesoscopic devices by deposition of perovskite material ($CH_3NH_3PbI_3$ or Cl/Br-doped $CH_3NH_3PbI_3$) onto a mesoporous TiO_2 layer coated on FTO glass and subsequent deposition of hole-transporting material (HTM) and Au counter electrode (CE).[10,14-17] The role of mesoporous TiO_2 layer in this device is accepting the photoexcited electrons from the perovskite and then transporting to the FTO. In addition to the mesoscopic device, the planar-type device, fabricated without employing the mesoporous TiO_2 layer, has also been demonstrated to show high photovoltaic performance, but planar-type devices require the use of Cl or Br-doped $CH_3NH_3PbI_3$, which exhibits significantly longer electron and hole diffusion lengths than the bare $CH_3NH_3PbI_3$.[5,18] Moreover, several reports indicate that the hysteresis in *J-V* scan, which is typically found in the planar-type device, can be alleviated by introducing mesoporous TiO_2 layer,[19-22] which seems to be caused by relatively larger contacting area between perovskite and TiO_2. Particularly, for the pure $CH_3NH_3PbI_3$-based device, mesoporous TiO_2 is regarded to be an essential scaffold for efficient collection of electrons from the perovskite. The optimal thickness of mesoporous TiO_2 layer is a few hundred nanometers because the thicker TiO_2 layer is not necessary due to extremely high extinction coefficient of $CH_3NH_3PbI_3$.

In mesoscopic perovskite solar cells, TiO_2 nanoparticles (NPs) are commonly used to form the mesoporous TiO_2 layer. On one hand, for the efficient injection of photoelectrons from perovskite to TiO_2, it is desirable to have mesoscopic TiO_2 layer with large surface area because it will increase the interfacial area between perovskite and TiO_2. For this purpose, smaller TiO_2 NPs will be suitable. On the other hand, for the complete infiltration of perovskite into the mesoporous TiO_2 structure, the pores in the TiO_2 layer needs to be sufficiently large and homogeneous in size without the presence of tiny pores. For this purpose, TiO_2 NPs of larger sizes will be favorable. In particular, we believe that the efficient pore-filling in the TiO_2 layer by perovskite is crucial for blocking the direct contact between TiO_2 and HTM and thus minimizing the loss of electrons via charge recombination between TiO_2 and HTM. In addition, for the efficient electron transport through the TiO_2 layer, it will be helpful to minimize the grain boundaries in the TiO_2 layer, which can be also reduced by using TiO_2 NPs of larger sizes. Thus, in order to optimize electron injection into and electron transport through the mesoscopic TiO_2 layer, the size of TiO_2 NPs and the resultant pore structure of the TiO_2 layer have to be controlled so that the two contradicting requirements discussed above can be compromised.

Besides the size of TiO_2 NPs, the shape of TiO_2 NPs also influences the pore structure as well as the connectivity among the NPs. Highly crystallized TiO_2 NPs in the anatase phase have often been synthesized by water-based hydrothermal reactions under basic conditions.[23-32] For instance, TiO_2 NPs formed in the presence of alkylamines have the sizes bigger than 100 nm with the shapes of octahedron, truncated octahedron, or elongated rod-like structures.[27-32] In this hydrothermal reaction, grain growth occurs rapidly due to the water solvent that expedites hydrolysis and sol-gel reaction of Ti-precursors as well as growth of TiO_2 nanocrystals. Moreover, alkylamines serve as a catalyst to facilitate the crystal growth, especially inducing anisotropic growth towards a specific crystallographic face,[24,27,29-32] resulting in the formation of TiO_2 NPs with the shapes of polygons or rod-like structures. The TiO_2 NPs of such anisotropic shapes tend to be stacked nonuniformly, leading to poor contacts among the NPs and undesirable pore structures, that is, the pores of inhomogeneous size and shape distributions. Instead, if the NPs of spherical or round-edge shape can be synthesized, the fabricated films will have greatly improved contacts and connectivity among the NPs as well as the pores of uniform sizes with good channel connectivity, which will be beneficial for the efficient infiltration of perovskite material into the mesoscopic TiO_2 layer. However, tailoring of TiO_2 NPs or design of mesoscopic TiO_2 structure for perovskite solar cells have scarcely been attempted thus far, in spite of their importance in determining the photovoltaic performances.[33,34]

For the first time, in this work, we synthesized single crystalline TiO_2 NPs of spherical shape by modifying the solvent system of conventional hydrothermal reaction.[35] This simple strategy has the effect of retarding the sol-gel reaction and the grain growth during the reaction, leading to the formation of spherical TiO_2 NPs with the size controllable in the range of 30–65 nm. Then, the prepared TiO_2 NPs were successfully used for fabricating mesoporous TiO_2 layers for the highly efficient perovskite solar cells. In addition, we systematically investigated the effects of NP size on the photovoltaic properties of perovskite solar cells by applying time-resolved spectroscopic techniques.[5,6,33, 36-42]

Results and discussion

To control the size and shape of TiO_2 NPs, we modified the solvent system for the typical hydrothermal reaction. Specifically, the solvent system of ethanol/water mixtures instead of pure water effectively retarded the sol-gel reaction and crystal growth during the hydrothermal process. Fig. 1 shows TEM images of as-prepared TiO_2 NPs synthesized by the hydrothermal reaction at 230 ^oC in the ethanol/water solvent mixture of various ethanol volume fractions (X_{EtOH}). In 90% water environment (X_{EtOH} = 0.1), as shown in Fig. 1a, a longish TiO_2 NP with the diameter of ~60 nm and the length of ~100 nm is formed, which is in agreement with previous studies.[27-31] With increasing X_{EtOH}, the sizes of the as-prepared TiO_2 NPs gradually decrease while their shapes change from the longish and angled structure to the spherical shape. With X_{EtOH} of 0.3, the prepared TiO_2 NP has slightly elongated and angled structure with the average diameter of 50 nm and length of 65 nm (termed NP65), as shown in Fig. 1b. In contrast, with X_{EtOH} of 0.5, 0.7, and 0.85, the prepared TiO_2 NPs are of spherical shapes with diameters of 50, 40, and 30 nm (termed NP50, NP40, and NP30, respectively), respectively, as shown in Fig. 1c–1e. Particularly, as seen in the low-magnification TEM image in Fig. 1f, NP50 is highly monodispersed spherical TiO_2 NPs that are well separated from each other without appreciable aggregation. We believe that such a large TiO_2 NP with spherical shape has never been reported thus far. In overall, sizes and shapes of TiO_2 NP are strongly dependent on X_{EtOH}, and the critical composition to achieve spherical morphologies is X_{EtOH} = 0.5–0.85. When X_{EtOH} becomes lower than 0.5, the NPs become gradually elongated, whereas their diameters do not change much. With X_{EtOH} higher than 0.85, the sol-gel reaction is difficult to control. Hence the prepared TiO_2 NPs are aggregated, with difficulty in the control of sizes and shapes.

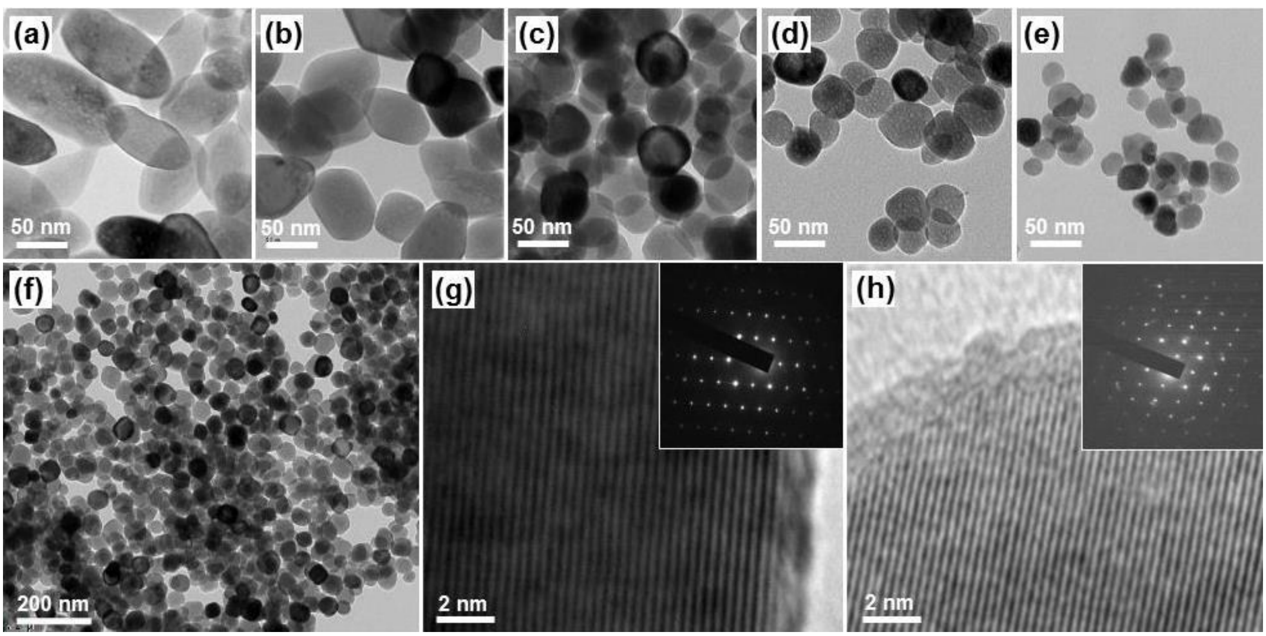

Fig. 1 TEM images of the as-prepared TiO_2 NPs under X_{EtOH} of a) 0.1, b) 0.3, c) 0.5, d) 0.7, and e) 0.85, which are denoted as NP100, NP65, NP50, NP40, and NP30, respectively. Low magfication TEM image for f) NP50 in c and high maginfication TEM images for g) NP65 in b and h) NP50 in c. Selected area electron diffraction (SAED) patterns, acquired from a single particle of NP65 and NP50, are shown in the insets of g and h, respectively.

To analyze the fringe patterns in a TiO_2 nanocrystal, we further magnified the TEM images of NP65 and NP50, as shown in Fig. 1g and 1h, respectively. The fringe spacing of NP65 was measured to be 0.35 nm, corresponding to the (101) plane of the anatase phase, indicating that the nanocrystal was grown along the (001) direction. Previously, it was reported that the presence of alkylamines such as diethylamine (DEA), which was also added to the solution in the present work, expedites the TiO_2 crystal growth during the hydrothermal reaction and especially promotes anisotropic growth to the (001) facet.[27-32] Therefore, the elongated structure of NP65, which was prepared under a water-rich environment, to the (001) direction is in good agreement with the previous reports.[30-32] In contrast, NP50 prepared under a X_{EtOH} of 0.5 has spherical morphology due to the retardation of the crystal growth by the presence of ethanol. Interestingly, it also exhibits uniform fringe patterns throughout a particle (see Fig. 1h), suggesting that individual NPs are single crystals, presumably resulting from isotropic grain growth. Selected area electron diffraction (SAED) patterns were obtained for single particles of NP65 and NP50, as shown in the insets of Fig. 1g and 1h, respectively. Uniform dot patterns were observed for both the elongated NP65 and the spherical NP50, confirming that both NPs are single crystals, regardless of the particle shape.

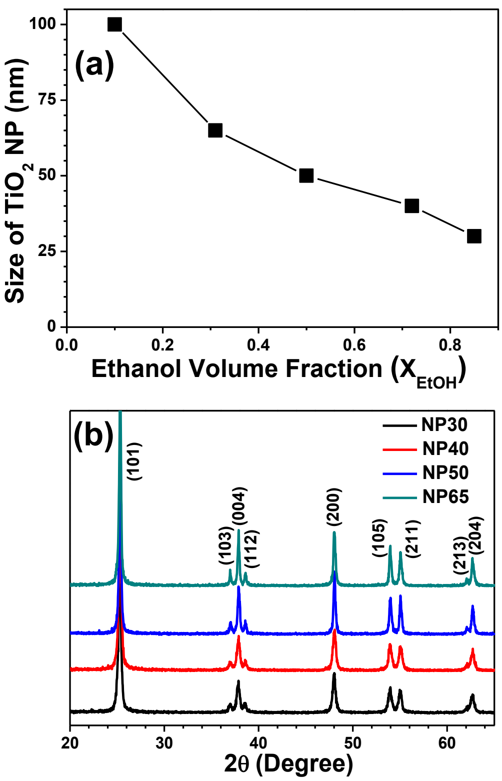

Fig. 2 a) Size variation of TiO_2 NPs as a function of X_{EtOH} in the solution mixture. b) XRD patterns for the as-prepared TiO_2 NPs with sizes of 30, 40, 50, and 65 nm.

Fig. 2a shows the size variation of TiO_2 NPs as a function of X_{EtOH} in the solution mixture used for the hydrothermal reaction. The diameter (or length) of the prepared NPs decreases gradually, as X_{EtOH} increases in the range of 0.1–0.85. The intense XRD peaks with narrow line widths in Fig. 2b indicate that all of the as-prepared TiO_2 NPs are in highly crystallized and pure anatase phase.

The TiO_2 NPs with the sizes of 30–65 nm were applied to the preparation of mesoporous photoelectrodes for $CH_3NH_3PbI_3$ perovskite solar cells. Specifically, we coated a mesoporous TiO_2 layer on the FTO glass by spin-coating TiO_2 paste containing NPs of a specific size and subsequently calcining at 500 ^oC. The scanning electron microscope (SEM) images in Fig. 3a show the cross-sections of various TiO_2 layers deposited on the FTO layer, and it can be seen that all the TiO_2 layers have the thicknesses in the range of 200–220 nm including a compact layer of ~10 nm thickness. The physical properties of the various TiO_2 layers, that is, surface areas of the NPs, layer thickness, average pore diameter (see Fig. 3b), and roughness factor (RF),[43,44] are listed in Table 1. As the size of TiO_2 NPs increases, the average diameter of the pores generated in the TiO_2 layer increases, whereas the RF of the TiO_2 layer decreases. Fig. 3c shows the cross-section of a NP50-based TiO_2 layer coated with $CH_3NH_3PbI_3$. The $CH_3NH_3PbI_3$ material seems to be uniformly infiltrated into the mesopores of the TiO_2 layer, and the thickness of a $CH_3NH_3PbI_3$ overlayer on the top of the TiO_2 is 100–200 nm. Fig. 3d shows the cross-section of a fabricated perovskite solar cell containing a NP50-based TiO_2 layer, where the thicknesses of spiro-OMETAD layer and an Au counter electrode are ~300 and ~60 nm, respectively.

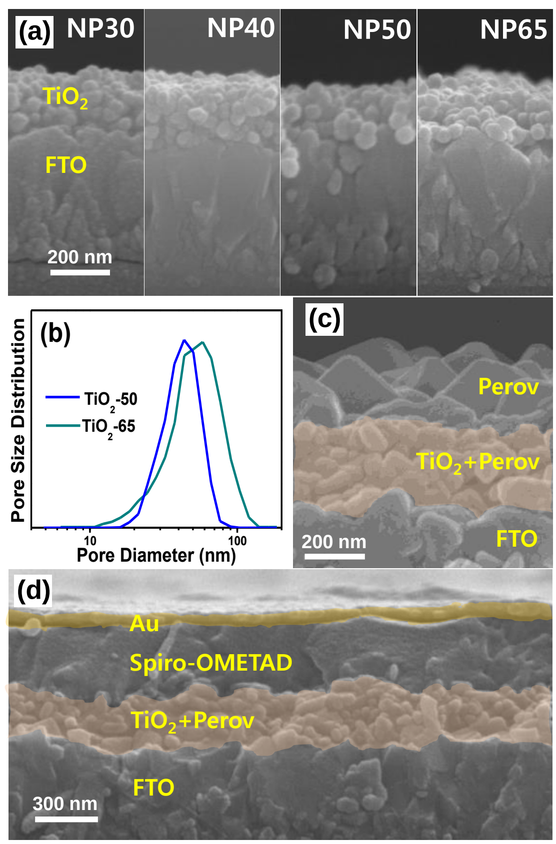

Fig. 3 a) Cross-sectional SEM images for the TiO_2 layers derived from various NPs. b) Pore size distributions for the TiO_2 layers derived from NP50 and NP65. Cross-sectional SEM images for c) $FTO/TiO_2/CH_3NH_3PbI_3$ and d) $FTO/TiO_2/CH_3NH_3PbI_3$/spiro-OMETAD/Au.

Table 1. Physical properties of several TiO_2 layers.

TiO_2 films	Surface area of TiO_2 NP [m^2g^{-1}]	Layer thickness [nm]	Average pore size [nm]	Roughness factor (RF)
TiO_2-30	57	210	24	23
TiO_2-40	40	220	34	18
TiO_2-50	34	200	45	13
TiO_2-65	28	220	56	11

The *J-V* curves of the perovskite solar cells, derived from NP30, NP40, NP50, and NP65 are shown in Fig. 4a, while the detailed parameters are listed in Table 2. Among various solar cells containing NPs of a specific size, the device using NP50 (termed PSC-50) shows the highest PCE (17.19%) with J_{SC} of 21.58 mA/cm^2, V_{OC} of 1,049 mV and *FF* of 0.759. With increase of the size from 30 nm to 50 nm, J_{SC} does not change much, but V_{OC} and *FF* increase significantly, as shown in Fig. 4b. However, with further increase of the TiO_2 NP size to 65 nm, V_{OC} and *FF* decrease, and thus the PCE also decreases down to 15.47%.

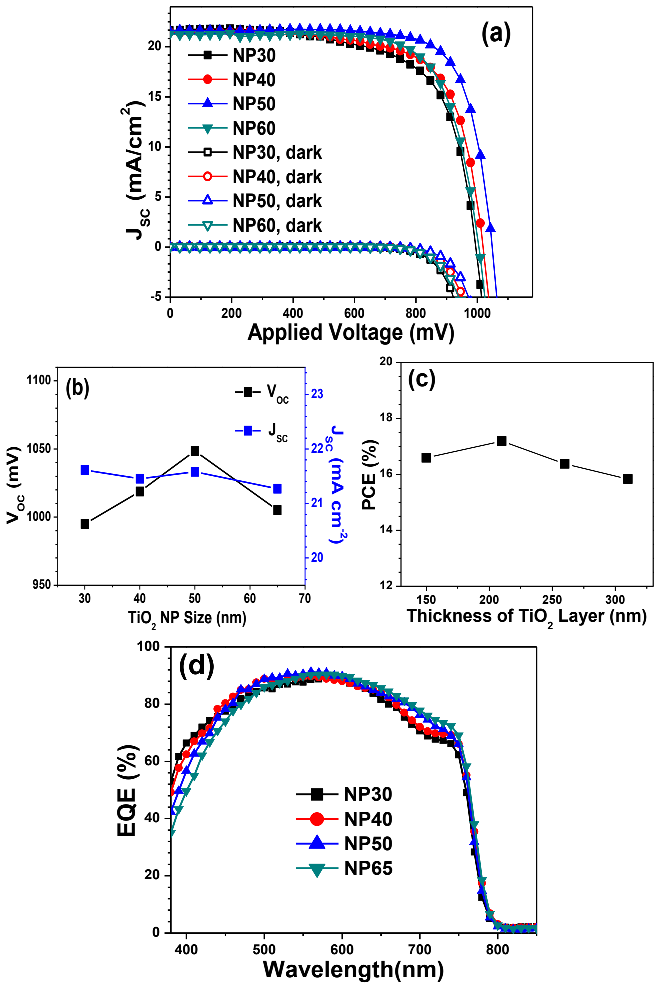

Fig. 4 a) J-V curves for the several perovskite solar cells. b) Change of V_{OC} and J_{SC} according to the TiO_2 NP size and c) change of PCEs for the PSC-50 depending on the thickness of TiO_2 layer. d) IPCE spectra for the several perovskite solar cells.

Dark current–voltage curves of the devices employing different TiO_2 NPs are also included in Fig. 4a. It is obvious that PSC-50 exhibits the lowest dark current at high bias voltage near 1,000 mV, which indicates that the current leakage of TiO_2 layer is minimized by employing NP50. The obtained result is compatible with the enhanced V_{OC} of PSC-50. To determine the optimum thickness of the TiO_2 layer for efficient solar cells, we varied thicknesses of TiO_2 layer in the PSC-50 in the range of 150-320 nm. As shown in Fig. 4c, the solar cell with a 200 nm-thick TiO_2 layer gives the highest PCE, while further increase of the TiO_2 layer thickness decreases the cell efficiency.

Table 2. J-V curve parameters of several perovskite solar cells employing TiO_2 NPs of various sizes.

Perovskite solar cells	V_{OC} [mV]	J_{SC} [mA cm^{-2}]	Fill factor [%]	PCE [%]
PSC-30	995	21.61	66.59	14.32
PSC-40	1029	21.45	69.74	15.24
PSC-50	1049	21.58	75.94	17.19
PSC-65	1005	21.27	72.35	15.47

Incident photon-to-current efficiency (IPCE) spectra of the various perovskite solar cells are shown in Fig. 4d. The integrated current densities calculated from the IPCE spectra correspond to the J_{SC} values, acquired from the *J-V* curves. The maximum external quantum efficiency (EQE) of PSC-50 is as high as 88%. At the wavelength around 700 nm, the EQEs of perovskite solar cells containing NP50 and NP65 (termed PSC-50 and PSC-65, respectively) are slightly higher than those of the cells employing NP30 or NP40 (termed PSC-30 and PSC-40, respectively). In contrast, at the wavelengths shorter than 450 nm, PSC-50 and PSC-65 showed significantly lower EQEs than PSC-30 or PSC-40, implying that the short-wavelength photons are not efficiently utilized in PSC-50 and PSC-65 probably due to larger light-scattering by bigger TiO_2 NPs. When comparing the IPCE spectra of PSC-30 and PSC-65, the area difference between the two spectra is larger at short wavelengths (EQE loss for PSC-65) than at long wavelengths (EQE gain for PSC-65). Therefore, the light-scattering effect enhanced for larger NPs is not responsible for enhancing the PCE of the perovskite solar cells.

In perovskite solar cells, the TiO_2 layer plays a role of transporting photo-excited electrons from perovskite to FTO. To optimize the efficiency of the electron transport, the TiO_2 layer needs to satisfy several criteria. First, the TiO_2 layer needs to have large surface area so that the contact area between perovskite and TiO_2 can be maximized. In this regard, smaller TiO_2 NP will be more favorable as building blocks of the TiO_2 layer. Second, the TiO_2 layer needs to have an efficient structure for the electron transport. That is, the grain boundaries and defects have to be minimized. For this purpose, larger TiO_2 NPs are favored. Third, the perovskite has to be completely infiltrated into the mesoporous network of the TiO_2 layer. If the TiO_2 surface is not completely covered with perovskite, the uncovered TiO_2 area can contact HTM directly, inducing the charge recombination between TiO_2 and HTM. Hence, for the efficient infiltration of perovskite phase into the TiO_2 layer, the pore size of TiO_2 layer has to be sufficiently large and uniform without the presence of tiny pores. In addition, regarding the shape of TiO_2 NPs, spherical morphology will be favorable for generating homogeneous mesopores.

As schematically illustrated in Fig. 5a, upon irradiation of solar light, photoexcited electrons generated in perovskite are injected into the conduction band (CB) of TiO_2. Then, the injected electrons diffuse through the TiO_2 layer to reach the FTO, while some of the electrons are lost by recombining with holes in the valence band (VB) of perovskite or the HOMO of HTM. These dynamic processes, that is, charge injection and charge transport, will be significantly influenced by mesoscopic structure of the TiO_2 layer. To examine the effect of mesoscopic TiO_2 structure on the charge dynamics in perovskite solar cells, we applied two types of time-resolved spectroscopic techniques. Firstly, to evaluate the efficiency of charge injection from perovskite to TiO_2, we measured time-resolved photoluminescence (TR-PL) for FTO/TiO_2/$CH_3NH_3PbI_3$ devices (without introducing HTM) that employ various TiO_2 NPs of a specific size. As can be seen in Fig. 5b and Table 3, the temporal decay of PL intensity becomes faster, as the size of the TiO_2 NPs decreases. In other words, the FTO/TiO_2/$CH_3NH_3PbI_3$ device containing NP30 exhibits the fastest TR-PL decay.

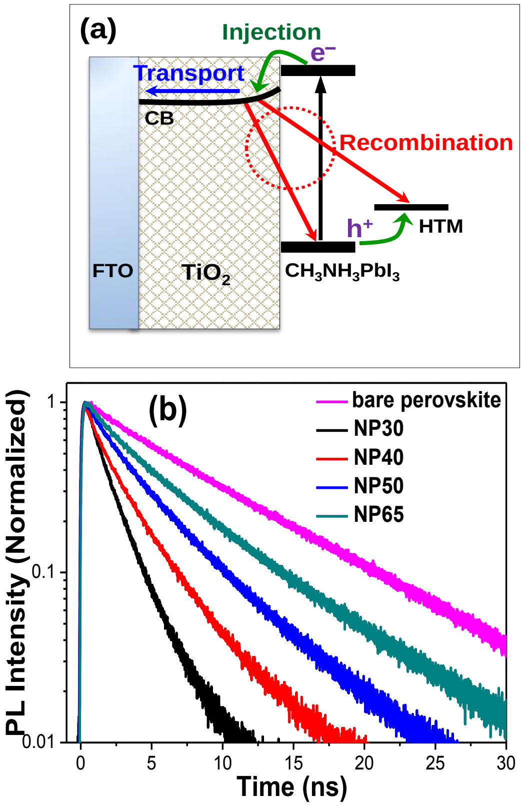

Fig. 5 a) A schematic diagram describing the charge transport and recombination pathway in the perovskite solar cell. b) TR-PL decays of the bare $CH_3NH_3PbI_3$ deposited on Pyrex glass and the FTO/TiO_2/$CH_3NH_3PbI_3$ devices employing NP30, NP40, NP50, and NP65. It can be clearly seen that the TR-PL decay is accelerated with the decrease of the size of TiO_2 NPs. The time resolution of the TR-PL measurement was ~190 ps.

The TR-PL decay of the perovskite device arises from quenching of PL intensity due to either (1) radiative relaxation of excited electrons back to the ground state of perovskite or (2) electron transport from perovskite to TiO_2. Because the radiative relaxation back to the ground state of perovskite occurs at a certain inherent rate (that corresponds to the TR-PL decay rate of bare $CH_3NH_3PbI_3$ shown in Fig. 5b, the acceleration of TR-PL decay with the decrease of TiO_2 NP size in the FTO/TiO_2/$CH_3NH_3PbI_3$ devices indicates more efficient injection of electrons from the perovskite to TiO_2. Therefore, we can infer that, as the TiO_2 NPs become smaller, the contact area among NPs becomes larger and the electron injection from perovskite to TiO_2 becomes more efficient.

Table 3. Charge transfer times (τ_{CT}) and charge transfer efficiencies (CTE) estimated from the PL lifetimes ($\tau_{interface}$) of FTO/TiO_2/$CH_3NH_3PbI_3$ samples employing TiO_2 NPs of various sizes.

Sample	$\tau_{interface}$ (ns)[a)]	τ_{CT} (ns)	CTE (%)
Bare $CH_3NH_3PbI_3$	8.7 ± 0.2[b)]	--	--
NP30/$CH_3NH_3PbI_3$	1.5 ± 0.1	1.8	82.7
NP40/$CH_3NH_3PbI_3$	1.9 ± 0.1	2.4	78.1
NP50/$CH_3NH_3PbI_3$	3.5 ± 0.1	5.6	59.4
NP65/$CH_3NH_3PbI_3$	4.2 ± 0.1	7.4	51.7

[a)]The PL lifetime of each $CH_3NH_3PbI_3$/TiO_2/FTO sample corresponds to the amplitude-weighted average lifetime of a multi-exponential decay fit; b)Time constant for the TR-PL decay of bare $CH_3NH_3PbI_3$ film.

Secondly, by applying the pulsed light-induced transient measurement (PLITM) technique, we measured the electron diffusion coefficient and the electron lifetime of the photo-injected electrons in the TiO_2 layer during the perovskite solar cell operation.[37-42] The electron diffusion coefficient, D_e, was determined by the equation, $D_e = L^2 / (2.35 \times \tau_c)$, where L is the thickness of the TiO_2 layer and τ_c is the time constant of a single-exponential fit to the transient photocurrent decay at the short-circuit condition. The D_e values as a function of J_{SC} are shown in Fig. 6a for various TiO_2 layers containing NPs of a specific size. We can see that D_e does not change significantly with respect to the size of TiO_2 NPs. This observation suggests that the electron diffusion through TiO_2 layer is sufficiently efficient regardless of the size of TiO_2 NPs, probably because individual NPs in the TiO_2 layers are fully interconnected by the calcination at 500 °C.

The electron lifetime, τ_e, was determined from a single-exponential fit of the decay of transient photocurrent at the open-circuit condition. The τ_e value represents the lifetime of photogenerated electrons that survive from charge recombination between the CB of TiO_2 and the VB of perovskite or HTM. The τ_e values measured as a function of J_{SC} are shown in Fig. 6b for various TiO_2 layers containing NPs of a specific size. We can see that τ_e changes significantly depending on the size of TiO_2 NPs. In particular, the τ_e value increases gradually as the size of NPs increases from NP30 to NP50 whereas NP65 has a smaller τ_e value than NP50. The dependence of τ_e on the NP size is in good agreement with the NP size dependence of PCE and V_{OC} shown in Fig. 4b. Thus, we can conclude that charge recombination, which determines τ_e, is the most crucial factors that govern the photovoltaic performance of perovskite solar cells.

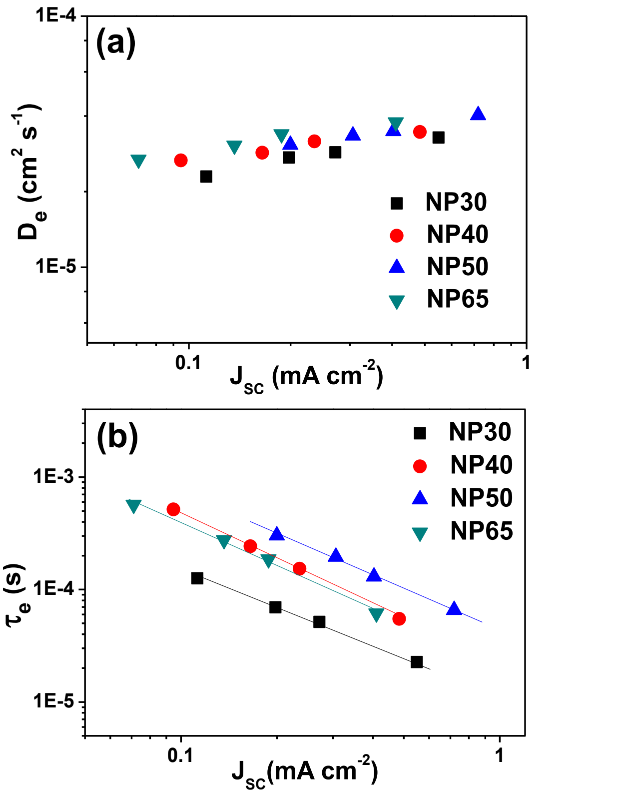

Fig. 6 Plots of a) the electron diffusion coefficient (D_e) vs. J_{SC} and b) the electron lifetime (τ_e) vs. J_{SC} for the perovskite solar cells employing NP30, NP40, NP50, and NP65.

Then, why does the TiO_2 layer consisting of NP50 exhibit the longest τ_e and thus the lowest charge recombination rate? As discussed above, we propose that charge recombination is governed by how well perovskite infiltrates into mesopores in the TiO_2 layer. With poor infiltration of perovskite into the TiO_2 layer, the TiO_2 material can contact the HTM directly, resulting in the recombination of electrons in TiO_2 with holes in HTM. For the efficient infiltration of perovskite into the TiO_2 layer, the pores in the TiO_2 layer have to be sufficiently large and uniform in size without the presence of tiny pores. As shown in Fig. 3b, the TiO_2 layer consisting of NP50 has relatively homogeneous mesopores with the average pore size of 45 nm, which is significantly larger than that of the NP30-layer (28 nm) or the NP40-layer (36 nm). Although the NP65-layer has an average pore size (56 nm) significantly larger than other TiO_2 layers, it has a broader size distribution of pores, including the presence of narrow pores. NP65 has an angled oval-like shape due to relatively faster grain growth in the (001) direction and therefore the stacking of NP65 particles will be more irregular than other spherical NPs, leading to the pores of nonuniform sizes and shapes. Thus, the TiO_2 layer consisting of NP50 has the most effective pore structure as a result of the optimum combination of large pore size and uniform distribution of pore size, thus accounting for the suppressed charge recombination and the best photovoltaic performance of PSC-50.

We note that PSC-50 consisting of spherical NP50 particles shows relatively little hysteresis in the *J-V* measurement as shown in Fig. 7a. The PCEs for forward and reverse scans were 15.76% and 16.60%, respectively, which are very similar to each other. Moreover, PSC-50 exhibits highly reproducible photovoltaic properties. As shown in Fig. 7b, about 70% of the prepared photovoltaic devices exhibit the PCEs in the range of 16–18 %. We infer that the highly reproducible PCE of PSC-50 originates from efficient infiltration of perovskite into the mesoporous TiO_2 structure. As we demonstrated, NP50 forms a network of large and uniform pores and thus provides the best morphology for fabricating mesoporous photoelectrode for efficient perovskite solar cells.

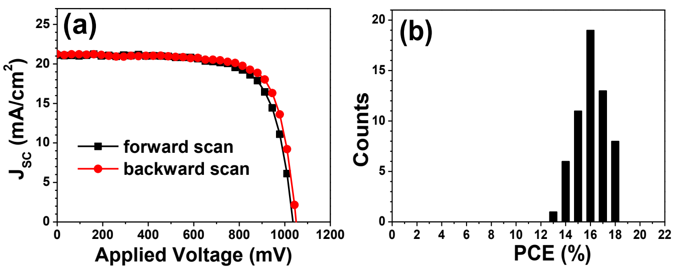

Fig. 7 a) J-V curves of a PSC-50 acquired by forward and backward scans with a scan rate of 100 mV s^{-1}. b) PCE distributions for the 58 devices of PSC-50.

Conclusions

Spherical TiO_2 NPs with diameters of 30, 40, 50, and 65 nm were selectively prepared and adopted to construct perovskite solar cells. The PSC-50 that employs NP50 exhibited the highest PCE of 17.19% with J_{SC} of 21.58 mA/cm^2, V_{OC} of 1.049 V, and *FF* of 0.759, while significant increase in V_{OC} and *FF*, rather than J_{SC}, is responsible for the increase of PCE. The IPCE spectra indicate that higher PCE of PSC-50 does not arise from the light-scattering effect. Time-resolved PL measurement for the FTO/TiO_2/perovskite devices shows the acceleration of the TR-PL decay with the decrease of the size of TiO_2 NPs, suggesting that larger TiO_2/perovskite contact area is favorable for efficient electron injection from perovskite to TiO_2. With respect to the size of TiO_2 NPs, the D_e value does not change much whereas τ_e value changes significantly. PSC-50 exhibited the longest τ_e, which originates from the effective pore structure in the TiO_2 layer and the suppressed charge recombination. The dependence of τ_e on the NP size is in good agreement with the NP size dependence of PCE and V_{OC}, suggesting that recombination is the critical factor that determines the photovoltaic performance of perovskite solar cells.

Experimental details

Synthesis of TiO_2 NPs

In a typical synthesis, 0.05 mol titanium isopropoxide (TTIP, Aldrich) was added to the solution containing 0.10 mol triethanolamine (TEOA, Aldrich) and 10 ml ethanol while stirring. The neat yellowish solution without any precipitation was then formed, indicating the formation of stabilized TTIP-TEOA complex. In a separated beaker, 0.02 mol diethylamine (DEA, Aldrich) was dissolved in 100 mL of water-ethanol mixture in stoichiometric ratio. It was then added dropwise to the Ti precursor solution, while vigorous stirring. Ethanol volume fraction (X_{EtOH}) in the reaction mixture for hydrothermal reaction was varied to control the size of TiO_2 NP. Typically, to prepare 50 nm-sized TiO_2 NP, the total amount of added ethanol was 55 mL (X_{EtOH} = 0.5). The resultant mixture in a clear pale yellow color was stirred for 6 h, and then transferred to glass-lined hydrothermal bomb made of titanium. The hydrothermal reaction was initially carried out at 100 ^oC for 4 h and then at 230 ^oC for 6 h. The prepared TiO_2 NP present in the solution was collected by centrifugation, washed with ethanol several times, and then dried in vacuum at 50 ^oC.

Fabrication of $CH_3NH_3PbI_3$ perovskite solar cells

As a TiO_2 compact layer, approximately 10 nm-thick Ti film was deposited on the patterned FTO glass (Pilkington, TEC8) by an RF magnetron sputtering system (A-Tech system, Korea), followed by oxidation at 500 ^oC for 30 min in air. Mesoporous TiO_2 layer with approximately 180 nm thickness was then spin-coated at 5,000 rpm for 30 s, using the prepared TiO_2 pastes, derived from various TiO_2 NPs. The coated films were then heated at 500 ^oC for 30 min. $CH_3NH_3PbI_3$ layer was deposited by two step method reported in the literature.[10] PbI_2 solution in N,N-dimethylformamide (462 mg/mL) kept at 70 ^oC was coated on the porous TiO_2 films by spin coating at 6,000 rpm for 60 s. It was dried at 70 ^oC for 30 min, and then cooled down to room temperature. The film was immersed in a CH_3NH_3I 2-propanol solution (10 mg/mL) for 20 s, and washed by 2-propanol, followed by drying at 70 ^oC for 15 min. The HTM layer was then coated by spin coating at 4000 rpm for 30 s using the solution consisting of 72.3 mg of spiro-OMETAD [2,29,7,79-tetrakis(N,N-di-p-methoxyphenylamine)-9,9-spirobifluorene] in 1 mL of chlorobenzene, 28.8 μL of 4-tert-butylpyridine, 17.5 μL of lithium bis(trifluoromethylsulphonyl) imide in 1 mL of acetonitrile, and 29 μL of tris(2-(1H-pyrazol-1-yl)-4-tert-butylpyridine) cobalt(III) bis(trifluoromethylsulphonyl) imide 1 mL acetonitrile. Au layer with a thickness of 60 nm was deposited by thermal evaporator (Korea Vacuum Tech.) to form the back contact. The active area of the device was defined by a metal mask with a size of 0.30 cm^2.

Characterizations

The morphologies of the prepared TiO_2 NPs were examined by transmission electron microscopy (TEM) using a JEOL Model JEM2100F operated at 200 kV. Cross-sectional images of TiO_2 films and devices were monitored by field-emission scanning electron microscopy (SEM, Hitachi S4300). P-V measurements were performed using a Keithley model 2400 source measurement unit. A 300 W Xenon lamp (Spectra-Physics) was used as the light source and the light intensity was adjusted using an NREL-calibrated Si solar cell equipped with a KG-5 filter for approximating AM 1.5 G one sunlight intensity. The incident photon to current efficiency (IPCE) spectra was measured as a function of wavelength from 400 to 900 nm using a specially designed IPCE system (PV Measurements, Inc.).

Time-resolved spectroscopic analyses

Time-resolved photoluminescence (TR-PL) was measured using a time-correlated single photon counting (TCSPC) spectrometer (FluoTime 200, PicoQuant). Film samples of FTO/TiO_2/perovskite were excited by 100-ps laser pulses of 390 nm center wavelength through FTO glass (that is, back illumination) and the emission from $CH_3NH_3PbI_3$-sensitized solar cells was collected at the wavelength of 760 nm. The temporal resolution of the TR-PL measurement was ~190 ps. The electron diffusion coefficient (D_e) and electron life time (τ_e) were measured by a home-made pulsed light-induced transient measurement (PLITM) of photocurrent equipment.[37-42] To obtain the transient photocurrent, the laser pulse (λ = 532 nm, pulse duration = 7 ns, LCS-DTL-314QT, Laser-Export) was irradiated from the counter electrode side, while the bias light (Coherent, LabLaser, λ=635 nm) was illuminated from the working electrode side. The electron diffusion coefficients (D_e) of TiO_2 layers were determined at the short-circuit condition, whereas the lifetimes of photogenerated electrons (τ_e) were determined at the open-circuit condition. The measurements were repeated while the intensity of the bias light was varied.

Acknowledgements

This work was supported by the Pioneer Research Program (2012-0001065), and the Korea Center for Artificial Photosynthesis (KCAP) funded by the Minister of Science, ICT and Future Planning (MSIP) through the National Research Foundation of Korea (Project No. 2009-0093884).

Notes and references

[a] Department of Chemistry and Chemical Engineering, Inha University, Incheon 402-751 Korea. *E-mail:* wanin@inha.ac.kr
[b] Department of Chemistry and Chemical Engineering, Inha University, Incheon 402-751 Korea. *E-mail:* jkim5@inha.ac.kr

1 H.-S. Kim, C.-R. Lee, J.-H. Im, K.-B. Lee, T. Moehl, A. Marchioro, S.-J. Moon, R. Humphry-Baker, J.-H. Yum, J. E. Moser, M. Grätzel and N.-G. Park, *Sci. Rep*., 2012, **2**, 591.
2 M. M. Lee, J. Teuscher, T. Miyasaka, T. N. Murakami and H. J. Snaith, *Science*, 2012, **338**, 643–647.
3 J. H. Noh, S. H. Im, J. H. Heo, T. N. Mandal and S. I. Seok, *Nano Lett*., 2013, **13**, 1764–1769.
4 J. H. Heo, S. H. Im, J. H. Noh, T. N. Mandal, C.-S. Lim, J. A. Chang, Y. H. Lee, H.-J. Kim, A. Sarkar, M. K. Nazeeruddin, M. Grätzel and S. I. Seok, *Nat. Photonics*, 2013, **7**, 486–492.
5 S. D. Stranks, G. E. Eperon, G. Grancini, C. Menelaou, M. J. P. Alcocer, T. Leijtens, L. M. Herz, A. Petrozza and H. J. Snaith, *Science*, 2013, **342**, 341–344.
6 T. J. Savenije, C. S. Ponseca, Jr., L. Kunneman, M. Abdellah, K. Zheng, Y. Tian, Q. Zhu, S. E. Canton, I. G. Scheblykin, T. Pullerits, A. Yartsev and V. Sundström, *J. Phys. Chem. Lett.*, **5**, 2189–2194.
7 C. Wehrenfennig, G. E. Eperon, M. B. Johnston, H. J. Snaith and L. M. Herz, *Adv. Mater.*, 2014, **26**, 1584–1589.
8 V. D'Innocenzo, G. Grancini, M. J. P. Alcocer, A. R. S. Kandada, S. D. Stranks, M. M. Lee, G. Lanzani, H. J. Snaith and A. Petrozza, *Nat. Commun.*, 2014, **5**, 4586.
9 H. Zhou, Q. Chen, G. Li, S. Luo, T.-B. Song, H.-S. Duan, Z. Hong, J. You, Y. Liu and Y. Yang, *Science*, 2014, **345**, 542–546.

10 J. Burschka, N. Pellet, S.-J. Moon, R. Humphry-Baker, P. Gao, M. K. Nazeeruddin and M. Grätzel, *Nature*, 2013, **499**, 316–319.

11 M. Liu, M. B. Johnston and H. J. Snaith, *Nature*, 2013, **501**, 395-398.

12 D. Y. Liu and T. L. Kelly, *Nat. Photonics*, 2014, **8**, 133–138.

13 J. T. W. Wang, J. M. Ball, E. M. Barea, A. Abate, J. A. Alexander-Webber, J. Huang, M. Saliba, I. Mora-Sero, J. Bisquert, H. J. Snaith and R. J. Nicholas, *Nano Lett.*, 2014, **14**, 724–730.

14 N. J. Jeon, J. H. Noh, Y. C. Kim, W. S. Yang, S. Ryu and S. I. Seok, *Nat. Mater.*, 2014, **13**, 897–903.

15 J.-H. Im, I.-H. Jang, N. Pellet, M. Grätzel and N.-G. Park, *Nat. Nanotechnol.*, 2014, **9**, 927–932.

16 J.-W. Lee, D.-J. Seol, A.-N. Cho and N.-G. Park, *Adv. Mater.*, 2014, **26**, 4991–4998.

17 N. J. Jeon, J. H. Noh, W. S. Yang, Y. C. Kim, S. Ryu, J. Seo and S. I. Seok, *Nature*, 2015, **517**, 476–480.

18 G. Xing, N. Mathews, S. Sun, S. S. Lim, Y. M. Lam, M. Grätzel, S. Mhaislkar and T. C. Sum, *Science*, 2013, **342**, 344–347.

19 R. S. Sanchez, V. Gonzalez-Pedro, J.-W. Lee, N.-G. Park, Y. S. Kang, I. Mora-Sero and J. Bisquert, *J. Phys. Chem. Lett.*, 2014, **5**, 2357–2363.

20 H.-S. Kim and N.-G. Park, *J. Phys. Chem. Lett.*, 2014, **5**, 2927-2934.

21 H. J. Snaith, A. Abate, J. M. Ball, G. E. Eperon, T. Leijtens, N. K. Noel, S. D. Stranks, J. T. Wang, K. Wojciechowski and W. Zhang, *J. Phys. Chem. Lett.*, 2014, **5**, 1511–1515.

22 H.-W. Chen, N. Sakai, M. Ikegami and T. Miyasaka, *J. Phys. Chem. Lett.*, 2015, **6**, 164–169.

23 T. Sugimoto, K. Okada and H. Itoh, *J. Colloid Interface Sci.*, 1997, **193**, 140-143; T. Sugimoto, X. Zhou and A. Muramatsu, *J. Colloid Interface Sci.*, 2003, **259**, 43–52.

24 X. Chen and S. S. Mao, *Chem. Rev.*, 2007, **107**, 2891-2959.

25 X. Han, B. Zheng, J. Ouyang, X. Wang, Q. Kuang, Y. Jiang, Z. Xie and L. Zheng, *Chem. Asian J.*, 2012, **11**, 2538–2542.

26 C.-T. Dinh, T.-D. Nguyen, F. Kleitz and T.-O. Do, *ACS Nano*, 2009, **3**, 3737–3743.

27 G. Liu, H. G. Yang, J. Pan, Y. Q. Yang, G. Q. Lu and H.-M. Cheng, *Chem. Rev.*, 2014, **114**, 9559–9612.

28 C. Matteo, R. G. Thomas and B. M. Christopher, *Chem. Rev.*, 2014, **114**, 9319–9345.

29 T. Sugimoto, K. Okada and H. Itoh, *J. Colloid Interface Sci.*, 2003, **259**, 53–61.

30 J.-W. Shiu, C.-M. Lan, Y.-C. Chang, H.-P. Wu, W.-K. Huang and E. W.-G. Diau, *ACS Nano*, 2012, **6**, 10862–10873.

31 N. Roy, Y. Sohn and D. Pradhan, *ACS Nano*, 2013, **7**, 2532–2540.

32 H. J. Yun, H. Lee, J. B. Joo, W. Kim and J. Yi, *J. Phys. Chem. C*, 2009, **113**, 3050–3055.

33 Q. Shen, Y. Ogomi, J. Chang, S. Tsukamoto, K. Kukihara, T. Oshima, N. Osada, K. Yoshino, K. Katayama, T. Toyoda and S. Hayase, *Phys. Chem. Chem. Phys.*, 2014, **16**, 19984–19992.

34 G. Murugadoss, G. Mizuta, S. Tanaka, H. Nishino, T. Umeyama, H. Imahori and S. Ito, *APL Mater.*, 2014, **2**, 081511.

35 S. Y. Chae, M. K. Park, S. K. Lee, T. Y. Kim, S. K. Kim and W. I. Lee, *Chem. Mater.*, 2003, **15**, 3326–3331.

36 T. Leijtens, G. E. Eperon, S. Pathak, A. Abate, M. M. Lee and H. J. Snaith, *Nat. Commun.*, 2013, **4**, 2885.

37 J. van de Lagemaat and A. J. Frank, *J. Phys. Chem. B*, 2001, **105**, 11194–11205.

38 K. D. Benkstein, N. Kopidakis, J. van de Lagemaat and A. J. Frank. *J. Phys. Chem. B*, 2003, **107**, 7759–7767.

39 N. Kopidakis, K. D. Benkstein, J. van de Lagemaat and A. J. Frank, *J. Phys. Chem. B*, 2003, **107**, 11307–11315.

40 S. Nakade, T. Kanzaki, W. Kubo, T. Kitamura, Y. Wada and S. Yanagida, *J. Phys. Chem. B*, 2005, **109**, 3480–3487.

41 Y. J. Kim, K. H. Kim, P. Kang, H. J. Kim, Y. S. Choi and W. I. Lee, *Langmuir*, 2012, **28**, 10620–10626.

42 K. H. Kim, J. H. Moon, E. Y. Kim, H. J. Kim, S. H. Jang and W. I. Lee, *J. Mater. Chem.*, 2012, **22**, 11179–11184.

43 K. Shankar, J. I. Basham, N. K. Allam, O. K. Varghese, G. K. Mor, X. Feng, M. Paulose, J. A. Seabold, K.-S. Choi and C. A. Grimes, *J. Phys. Chem. C*, 2009, **113**, 6327–6359.

44 K. Shankar, G. K. Mor, H. E. Prakasam, S. Yoriya, M. Paulose, O. K. Varghese and C. A. Grimes, *Nanotechnol.*, 2007, **18**, 065707.

Graphical Abstract

50 nm-sized spherical TiO_2 nanocrystal for highly efficient mesoscopic perovskite solar cells

Sang Do Sung, Devi Prashad Ojha, Ji Su You, Joori Lee, Jeongho Kim and Wan In Lee

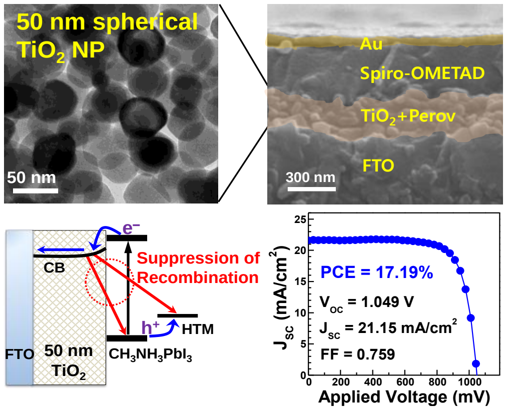

A novel 50 nm-sized spherical TiO_2 NP, prepared by a hydrothermal reaction, has been demonstrated to be a key component in fabricating highly efficient perovskite solar cells.